Radiation resistance of duplex stainless steel under proton irradiation: Correlation between microstructural evolution and nano-mechanical properties

Hyun Joon Eom[1], Sumin Kim[1], Chaewon Kim[2], Chaewon Jeong[1], Ye-jin Kweon[1], Changheui Jang[1,*]
[1]*Dept. of Nuclear and Quantum Engineering, KAIST, Daejeon, Rep. of Korea*
[2]*Korea Atomic Energy Research Institute, Daejeon, Rep. of Korea*
[*]*Corresponding Author: chjang@kaist.ac.kr*

***Keywords : Duplex stainless steel, Proton irradiation, Nano-indentation, B2-NiAl, γ'-precipitates**

1. Introduction

FeCrAl alloys have been considered as promising candidates for structural materials in various nuclear reactors due to their excellent corrosion resistance and mechanical properties, particularly in high-temperature steam environments or light water rector environment [1, 2]. However, duplex stainless steels have limitations in their use in the next-generation nuclear systems with higher operating temperature and higher levels of neutron irradiation. In particular, austenitic phase is susceptible to void swelling under irradiation, leading to unexpected mechanical degradation during operation [3]. Meanwhile, the spinodal decomposition in ferritic phase can cause embrittlement under long-term thermal exposure [4]. Furthermore, the requirement of reducing thickness to mitigate the neutronics penalty [5] increases the risk of structural instability and mechanical degradation in thin-walled components in nuclear reactors [6, 7].

In this regard, our research group has developed new type of duplex stainless steel (Alumina-forming Duplex Stainless Steel, ADSS), by incorporating a high Al content balanced with Ni content, stabilizing the ferritic and austenitic phases, respectively [8]. In addition, the combination of Al and Ni content leads to the formation of fine B2-NiAl precipitates in both austenitic and ferritic phases, which enhances the high-temperature mechanical properties and acts as Al reservoir to facilitate the formation of alumina under specific environments [9]. Moreover, B2-NiAl precipitates improve mechanical properties through Orowan model-based precipitate strengthening [10], thereby contributing to the long-term performance of these Fe-based alloys in nuclear reactors. However, their role in enhancing radiation resistance remains unexplored, and further investigation is required to understand their behavior under irradiation.

In this study, radiation resistance of ADSS was evaluated through microstructural analyses and nano-indentation tests under proton irradiation. In particular, the microstructural changes in austenitic and ferritic phase after proton irradiation were compared, and their correlation with nano-indentation test results was discussed to better understand the radiation-induced microstructural evolutions in this developed duplex stainless steel.

2. Methods and Results

2.1. Material and sample preparation

For this developed alloy with the target chemical composition, a casting ingot of 1.2kg was made by vacuum arc melting (VAR) and its accurate chemical composition was analyzed through the inductively coupled plasma atomic emission spectroscopy (ICP-AES) as shown in **Table 1**. After casting, the ingot was initially forged at 1100 ℃, followed by a 5-pass rolling with a total thickness reduction of 90 %. Before the first pass, the material was re-heated to 1100 ℃ for 10 min, while each subsequent pass was preceded by re-heating at the same temperature for 1 min.

Table 1 The chemical composition of ADSS (ICP-AES – KS D 1804/1803)

	Chemical composition (wt.%)							
	Fe	Ni	Cr	Al	Nb	Mn	C	Si
ADSS	Bal.	19.2	16.76	5.84	0.33	0.84	0.087	0.11

2.2. Proton Irradiation test

The ADSS fabricated through the above-mentioned process was cut into specimens of 20 mm × 2.5 mm × 1.5 mm by electrical discharging machining (EDM) for proton irradiation. Prior to the irradiation test, the specimens were mechanically polished with 0.05 μm colloidal silica. The irradiation test was then performed using 2 MeV proton at Michigan Ion Beam Laboratory (MIBL). The radiation damage profile (in dpa) was calculated using the Kinchin-Pease option in the SRIM-2013 code, assuming a displacement energy of 40 eV for all major elements, with the target damage of ~1.5 dpa and dose rate of 1×10^{-5} dpa/sec at depths up to ~1 μm, as shown in **Fig. 1**.

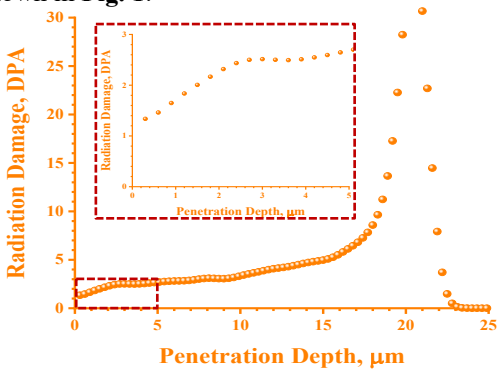

Fig. 1. The radiation damage (DPA) as a function of penetration depth (μm), using the Kinchin-Pease model in SRIM simulation code. The boxed region (~ 5

μm) with red dotted line is magnified to emphasize the radiation damage up to ~ 1 μm, which is the primary region for this study

2.3. Microstructural analysis

After proton irradiation, cross-sectional transmission electron microscopy (TEM) samples were prepared from both unirradiated and irradiated ADSS using a focused ion beam (FIB, Helios G4 FEI) technique. TEM analyses, including scanning TEM (STEM) with energy dispersive X-ray spectroscopy (EDS) and high-resolution TEM were performed using Titan cubed G2 60-300 FEI at 300 kV.

In the unirradiated ADSS, B2-NiAl precipitates are present in both regions with higher number density and larger average size in ferritic regions as previously reported in the journals from our research group. Additionally, the ferritic matrix contains a high density of nano-sized B2-NiAl precipitates (with the average diameter of ~17 nm).

In austenitic region, proton irradiation induces the dissolution of B2-NiAl precipitates, leading to the re-distribution of Ni and Al elements within austenitic matrix. As a result, formation of fine γ' precipitates are observed (**Fig. 2**), which is expected to contribute to the radiation hardening effect, as discussed in the nano-indentation test results in **Sec. 2.4**. On the other hand, in the ferritic region, large B2-NiAl precipitates remain, while nano-sized B2-NiAl precipitates within the ferritic matrix exhibit coarsening, with an increase in their average diameter to ~31 nm, as shown in **Fig. 3**. This microstructural evolution in the ferritic region is also expected to contribute to the radiation hardening observed in nano-indentation test results.

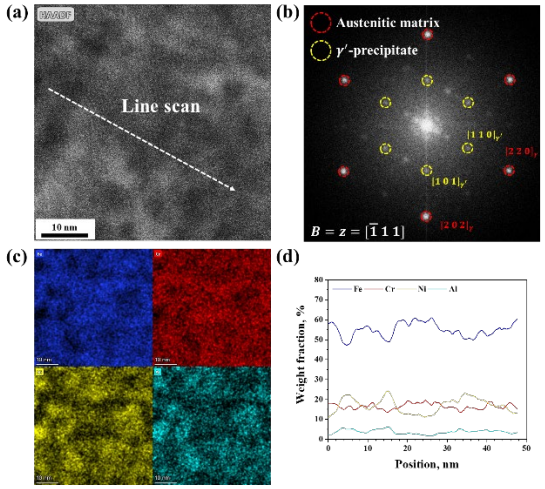

Fig. 2. (a) STEM micrograph with a white dotted line indicating the line scan region. Corresponding (b) fast Fourier transform (FFT) pattern showing diffraction spots of austenitic matrix and γ'-precipitates. (c) EDS mapping data for Fe (blue), Cr (red), Ni (yellow), and Al (sky-blue) element. (d) Line scanning profile (in wt.%) from the white dotted line in (a), showing the presence of γ'-precipitates, indicated by the fluctuation of Ni element distribution.

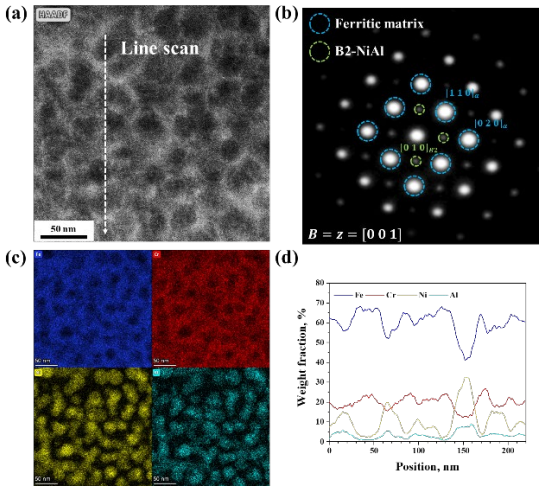

Fig. 3. (a) STEM micrograph with a white dotted line indicating the line scan region. Corresponding (b) fast Fourier transform (FFT) pattern showing diffraction spots of ferritic matrix and nano-sized B2-NiAl precipitates. (c) EDS mapping data for Fe (blue), Cr (red), Ni (yellow), and Al (sky-blue) element. (d) Line scanning profile (in wt.%) from the white dotted line in (a).

2.4. Nano-mechanical properties via nano-indentation

To evaluate the changes in mechanical properties within locally proton-irradiated region, a small-scale property measurement technique is required. Nano-indentation is a well-established method to assess the radiation hardening in the proton irradiated materials. Nano-indentation tests were performed on both unirradiated and irradiated specimens using a Hysitron TI-950 instrument equipped with a diamond Berkovich tip, aligned with the irradiation beam direction. The tip was calibrated using a standard quartz specimen before the tests. Indentation tests were arranged in 10×10 matrices with a separation distance of 10 μm to prevent plastic zone interaction between adjacent indents. The indentation tests were conducted using a nano-dynamic mechanical analysis (nano-DMA) mode, where the applied load was incrementally increased through 60 segments, each lasting for 2 sec until reaching a maximum load of 13,000 μN with oscillating frequency of 200 Hz. The maximum load was then held for another 2 sec, followed by the unloading process within 5 sec. The nano-indentation matrices were then analyzed using SEM to distinguish between austenitic and ferritic region, and the corresponding hardness data were separately processed for each region, as shown in **Fig. 4**a and **Fig. 4**c, respectively with the indentation hardness as a function of depth.

Meanwhile, the indentation size effect (ISE), which refers to the increase in measured hardness with decreasing indentation depth, must be accounted for when evaluating the nano-hardness changes in the irradiated austenitic and ferritic regions. In that sense, the degree of ISE can be estimated according to the well-known Nix-Gao model [11]:

$$H = H_0\left(1 + \frac{h^*}{h}\right)^{0.5} \cdots\cdots (1)$$

where H is the indentation hardness at a certain depth (h), measured from nano-DMA mode with the Oliver-Pharr

method [12], H_0 is the bulk hardness eliminating the effect of ISE, and h^* is the characteristic depth, representing the transition depth beyond which ISE becomes negligible. Therefore, to determine H_0, the square of the indentation hardness (H^2) was plotted as a function of inverse indentation depth ($1/h$), and a linear fitting was applied beyond h^* to extrapolate H_0, as shown in **Fig. 4**b and **Fig. 4**d.

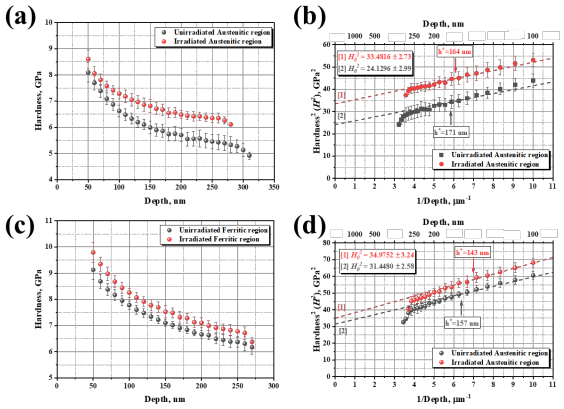

Fig. 4. Nano-hardness profiles as a function of indentation depth for (a) the austenitic region and (c) the ferritic region. The corresponding Nix-Gao plots, showing the square of the nano-hardness as a function of inverse indentation depth for (b) the austenitic region and (d) the ferritic region.

According to the above-mentioned process, the effect of proton irradiation on the bulk hardness of each region is summarized in **Fig. 5**. As discussed in the previous section (**Sec. 2.3**), the formation of fine γ'-precipitates in austenitic matrix leads to a significant increase in bulk hardness (~ 0.87 GPa), compared to the ferritic region (~ 0.31 GPa). This relatively small degree of radiation hardening in the ferritic region is likely attributed to the combination effect of coarsened nano-sized B2-NiAl precipitates in the ferritic matrix and the growth of Fe-Cr rich phase inside the large B2-NiAl precipitates during proton irradiation, which will be further analyzed through detailed microstructural investigations.

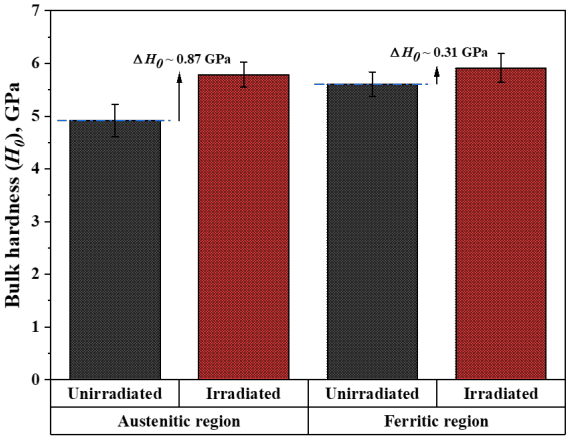

Fig. 5. Changes in bulk hardness (H_0) of the austenitic region and ferritic regions in ADSS after proton irradiation. The irradiation hardening values (ΔH_0) are also calculated and presented together.

3. Conclusion

In this study, a proton irradiation test (~ 1.5 dpa at the depth of ~ 1 μm) was conducted on the developed alloy from our research group (Alumina-forming duplex stainless steel, ADSS). By comparing the unirradiated and irradiated samples, the distinct microstructural evolution in the austenitic and ferritic regions was discussed in correlation with changes in nano-hardness using nano-indentation tests. While the coarsening of nano-sized B2-NiAl resulted in a small increase nano-hardness in the ferritic region, the formation of fine γ' precipitates in the austenitic matrix led to a relatively higher degree of radiation hardening effect. To elucidate underlying mechanism of this microstructural evolution after proton irradiation, further analyses should be performed.

REFERENCES

[1] K.A. Terrani, B.A. Pint, Y.-J. Kim, K. Unocic, Y. Yang, C. Silva, H. Meyer III, R.B. Rebak Uniform corrosion of FeCrAl alloys in LWR coolant environments, Journal of Nuclear Materials, vol. 479, pp. 36-47, 2016.
[2] K.A. Terrani, S.J. Zinkle, L.L. Snead Advanced oxidation-resistant iron-based alloys for LWR fuel cladding, Journal of Nuclear Materials, vol. 448, pp. 420-435, 2014.
[3] S.J. Zinkle, G. Was Materials challenges in nuclear energy, Acta Materialia, vol. 61, pp. 735-758, 2013.
[4] Y. Fan, T. Liu, L. Xin, Y. Han, Y.H. Lu, T. Shoji Thermal aging behaviors of duplex stainless steels used in nuclear power plant: A review, Journal of Nuclear Materials, vol. 544, pp. 152693, 2021.
[5] X. Wu, T. Kozlowski, J.D. Hales Neutronics and fuel performance evaluation of accident tolerant FeCrAl cladding under normal operation conditions, Annals of Nuclear Energy, vol. 85, pp. 763-775, 2015.
[6] Y. Yamamoto Development and quality assessments of commercial heat production of ATF FeCrAl tubes, vol. pp. 2015.
[7] H. Qu, Y. Lang, C. Yao, H. Chen, C. Yang The effect of heat treatment on recrystallized microstructure, precipitation and ductility of hot-rolled Fe–Cr–Al–REM ferritic stainless steel sheets, Materials Science and Engineering: A, vol. 562, pp. 9-16, 2013.
[8] H. Kim, H. Jang, G.O. Subramanian, C. Kim, C. Jang Development of alumina-forming duplex stainless steels as accident-tolerant fuel cladding materials for light water reactors, Journal of Nuclear Materials, vol. 507, pp. 1-14, 2018.
[9] X. Xu, X. Zhang, G. Chen, Z. Lu Improvement of high-temperature oxidation resistance and strength in alumina-forming austenitic stainless steels, Materials Letters, vol. 65, pp. 3285-3288, 2011.
[10] E. Orowan Symposium on internal stresses in metals and alloys, Institute of Metals, pp. 451-454, 1948.
[11] W.D. Nix, H. Gao Indentation size effects in crystalline materials: a law for strain gradient plasticity, Journal of the Mechanics and Physics of Solids, vol. 46, pp. 411-425, 1998.
[12] W.C. Oliver, G.M. Pharr An improved technique for determining hardness and elastic modulus using load and displacement sensing indentation experiments, Journal of materials research, vol. 7, pp. 1564-1583, 1992.